JET-P(96)17

ELMs as Ideal Interchange Instabilities near the Separatrix

W Kerner, O Pogutse, R van der Linden, B Schnuke.

JET Joint Undertaking, Abingdon, Oxfordshire, OX14 3EA, UK.

Preprint of a paper to be submitted for publication in
Plasma Physics and Controlled Fusion.

May 1996

ABSTRACT

The linear stability of the 'Scrape-off-Layer" (SOL) with respect to interchange-type modes is studied using the reduced MHD model and applying a ballooning approximation to the perturbations. 'Line-tying' boundary conditions are used at the target plates. Employing a metric determined by the magnetic field geometry, the influence of the X-point on stability is assessed. The effect of relevant parameters like X-point height, magnetic shear, and plasma shaping is qualitively determined. It is demonstrated that the calculations for experimental configurations and those based on an analytical equilibrium model yield good qualitative agreement.

It is shown that the SOL plasma just outside the separatrix can become unstable more easily (i.e. for lower pressure gradients) than the plasma just inside the separatrix where the magnetic well is stabilising. This finding is used to propose a model for the occurrence of giant ELMs. The interchange instability in the SOL acts as a precursor and is mainly localised near the X-point, but may also have a strong signature just above the outer midplane. The model provides a natural explanation for the occurrence of three different time scales in a giant ELM, and an estimate for the ELM repetition time is given. The scaling of the repetition time with power and current is shown to agree with experimental results.

1. INTRODUCTION

In tokamak H-mode experiments specific plasma activity is observed at the periphery of the plasma column in the form of edge localised modes (ELMs) [1]. The ELMs are MHD-type perturbations [2] with widely varying amplitudes and repetition rates. Following the classification of Doyle et al. [3] we concentrate on the so-called 'giant ELM', which occurs when the core plasma inside the separatrix is close to the ideal MHD ballooning limit. From MHD studies of ELMs in JET it has become clear that crucial elements are a local steepening of the edge pressure and current density profiles during the H-mode phase. Moreover, ELMs can occur at β values far below the ideal ballooning limit. This implies either that the MHD calculations are not complete or that the ELMs are not pure ideal modes (see e.g. [4]). In this paper, we analyse more carefully the first possibility by taking into account the role of the separatrix and especially of the X-point on plasma stability.

The tokamak edge plasma includes a part of the core plasma and a scrape-off-layer part a few Larmor radii inside and outside of the separatrix. These two regions have quite different topology with open and closed magnetic field lines. Due to MHD activity these two areas can interact. Therefore, the edge plasma plays a critical role in the behaviour of the entire plasma. At the initial stage of the tokamak discharge the modified resistive interchange and drift instabilities occur at the boundary resulting in large turbulent transport there. This turbulence can be transferred into the centre of the plasma column due to pumping mechanisms or due to the radial

mode structure. This plasma state corresponds to L-confinement. With increasing edge temperature the dissipative instabilities become weaker, the (turbulent) transport coefficients decrease and the gradients at the boundary get steeper. The profile of the pressure, (along with temperature and density) becomes increasingly more step-like. For large enough gradients Larmor radius stabilisation or shear flow stabilisation take place and turbulence is suppressed and the H-mode is set up [5]. Moreover, the development of a step-like pressure profile in the H-mode will lead to unstable MHD surface modes, which may explain the essential properties of the ELM phenomenon.

We artificially divide the stability problem near the plasma boundary into regions inside and outside the separatrix. These two regions are actually tightly connected but in order to gain some understanding it is useful to treat them separately. Inside the separatrix there is a magnetic well making the plasma more stable with increasing pressure, but outside this effect is absent, so that the plasma there can be more unstable than inside. Naturally the energy source outside the separatrix is much smaller than inside, but this region can trigger the main internal release of the free energy. An additional motivation is given by the fact that the stability of the plasma outside the separatrix is relevant in its own right for the SOL characteristics.

In section 2 we introduce a suitable system of coordinates, allowing substantial analytical simplification. Section 3 is devoted to the derivation of the MHD stability equation valid near the separatrix and includes a specific form of the energy principle, which can be useful for more general calculations. In section 4 numerical solutions of the stability equation in the region outside the separatrix are presented. In section 5 approximate analytical stability conditions are derived. In section 6 we apply these results to the description of ELM events and to estimates of the physical effects which follow from this model. In section 7 we briefly summarise and discuss the main results and conclusions. Appendix 1 contains a brief derivation and discussion of the coordinate system used, while in Appendix 2 the stability equation is cast in a simplified form valid near the X-point.

2. THE SYSTEM OF COORDINATES

For the description of the magnetic field geometry near the separatrix we choose the following orthogonal system of coordinates, where ρ is a flux surface label, ω an angle-like coordinate on the flux surface and φ the usual toroidal angle. The line element is given by:

$$ds^2 = h_\rho^2 d\rho^2 + h_\omega^2 d\omega^2 + R^2 d\varphi^2. \qquad (1)$$

In experimental JET equilibria these coordinates are constructed numerically. Then h_ρ and h_ω are given numerically at each grid point. For the analytical and, as will be demonstrated, for the numerical stability analysis near the separatrix a coordinate system can be used where the

coefficients h_ρ^2 and h_ω^2 have been taken from the straight cylinder model (see Appendix 1). Near the separatrix the metric coefficients can be written as

$$h_\rho^2 = \frac{y_0^2}{2^{5/2}} \cdot \frac{1}{\left[1-\cos(\omega)+\rho^2/2\right]^{1/2}}, \quad h_\omega^2 = \frac{y_0^2}{2^{5/2}} \cdot \frac{1}{\left[1-\cos(\omega)+\rho^2/2\right]^{1/2}}. \tag{2}$$

In the following we define $h = h_\rho = h_\omega$. We also introduce

$$R = R(\rho,\omega) = R_0 + x(\rho,\omega), \tag{3}$$

where

$$x(\rho,\omega) = (+/-)\frac{y_0}{\sqrt{2}}\left[-1+\cos(\omega)+\rho+\sqrt{2}\left(1-\cos(\omega)+\rho^2/2\right)^{1/2}\right]^{1/2}. \tag{4}$$

The expressions (2), (3) and (4) are correct near the separatrix $\rho << 1$, which in usual notation simply denotes that the distance from the separatrix has to be much less than the radius of the plasma column a. In an elongated plasma such as JET we distinguish the two semi axes a and b and have $b \approx y_0$. Near the X-point expressions (2), (3) can be further simplified to:

$$h^2 = \frac{y_0^2}{4} \cdot \frac{1}{\left[\omega^2+\rho^2\right]^{1/2}}, \tag{5}$$

$$x(\rho,\omega) = (+/-)\frac{y_0}{\sqrt{2}} \cdot \left[\rho+\left(\omega^2+\rho^2\right)^{1/2}\right]^{1/2}. \tag{6}$$

3. THE PERTURBED MHD EQUATIONS NEAR THE SEPARATRIX.

The stability equation for ideal MHD perturbations considered here is the usual ballooning equation [6], [7], [8] which is rewritten by taking into account the specific properties of the system of coordinates introduced:

$$\begin{aligned} &B_0\left(\frac{B_\omega}{h_\omega B_0}\frac{\partial}{\partial\omega}\right)\frac{1}{B_0}\left(\frac{nq}{h_\omega}\right)^2\left(1+\zeta^2\right)\left(\frac{B_\omega}{h_\omega B_0}\frac{\partial}{\partial\omega}\right)\tilde{\phi} - \gamma^2 C_A^{-2}\left(\frac{nq}{h_\omega}\right)^2\left(1+\zeta^2\right)\tilde{\phi} - \\ &\frac{4\pi}{RB_0}\left(\frac{nq}{h_\omega}\right)^2\frac{1}{h_\rho}\left(\frac{1}{h_\rho}\frac{\partial}{\partial\rho}\frac{R}{B_0} - \frac{\zeta}{h_\omega}\frac{\partial}{\partial\omega}\frac{R}{B_0}\right)\frac{dP_0}{d\rho}\tilde{\phi} = 0. \end{aligned} \tag{7}$$

Here we have used the eikonal [4] representation for the perturbed electrostatic potential:

$$\phi(t,\rho,\omega,\rho) = \tilde{\phi}(\rho,\omega)\cdot\exp\left(-\gamma t + in\int_{\omega_0}^{\omega} q(\rho,\omega')d\omega' - in\varphi\right), \tag{8}$$

where n is the toroidal mode number, q is the local safety factor, and ω_0 is an arbitrary parameter which has to be chosen so that the maximum growth rate is obtained [6]. The basic assumption is that the perturbation is localised at a field line (nq>>1) and that small terms of the order of B_p^2 / B_t^2 are neglected. The safety factor is given by

$$q = q(\rho,\omega) = \frac{B_0 h_\omega}{B_\omega R}, \tag{9}$$

and

$$\zeta = \zeta(\rho,\omega,\omega_0) = \frac{h_\omega}{h_\rho}\left(\frac{\partial}{\partial\rho}\int_{\omega_0}^{\omega} q(\rho,\omega')d\omega'\right)/q, \tag{10}$$

is a quantity that characterises the magnetic shear in the equilibrium. In Figure 1 the derivatives $x_\rho = \partial x/\partial\rho$ and $x_\omega = \partial x/\partial\omega$ are displayed. These characterise the curvature of the magnetic field lines.

The equations $\mathrm{div}\vec{B} = 0$ and $\mathrm{rot}\vec{B} = 0$ define the dependence of the components of the magnetic field on the poloidal coordinate ω:

$$B_\omega = B_\omega(\rho,\omega) = B_\omega(\rho,\pi)\cdot\frac{h_\rho(\pi)R(\pi)}{h_\rho(\rho,\omega)R(\rho,\omega)}, \tag{11}$$

and

$$B_0 = B_0(\rho,\omega) = B_0(\pi)\cdot\frac{R(\pi)}{R(\rho,\omega)}. \tag{12}$$

Equation (7) also can be derived from a simplified energy principle [9]. This principle can be written in vector form as a sum of the kinetic and potential energy:

$$E = T + W =$$

$$\gamma c^2\int\frac{n_0 M}{B_\varphi^2}(\nabla_\perp\phi)^2 dV - \frac{c^2}{\gamma}\int\frac{1}{RB_\varphi}[\nabla\phi x\nabla P_0]_\varphi\left[\nabla\phi x\nabla\frac{R}{B_\varphi}\right]_\varphi dV +$$

$$\frac{c^2}{4\pi\gamma}\int\frac{1}{R^2}\left[\nabla_\perp(R\nabla_{||}\phi)\right]^2 dV - \frac{c}{\gamma}\int\frac{j_\varphi}{RB_\varphi}\left[\nabla\phi x\nabla(R\nabla_{||}\phi)\right]_\varphi dV, \tag{13}$$

with

$$dV = h_\rho h_\omega R d\rho d\omega d\varphi. \tag{14}$$

In the right hand side of equation (13) the first term describes the inertia of the plasma, the second one represents curvature effects, the third term describes the Alfven waves and the last one accounts for the equilibrium current effects, and does not play a role for ballooning modes. In the ballooning approximation (8) (with nq >> 1) this expression can be simplified to (the term with the current disappears in this approximation):

$$\begin{aligned} E = \gamma c^2 \int \frac{n_0 M}{B_\varphi^2}\left(\frac{nq}{h}\right)^2\left(1+\zeta^2\right)\left|\tilde{\phi}\right|^2 dV + \\ \frac{c^2}{\gamma}\int \frac{1}{RB_\varphi}\frac{1}{h^2}\left(\frac{\partial}{\partial\rho}\frac{R}{B_\varphi} - \zeta\frac{\partial}{\partial\omega}\frac{R}{B_\varphi}\right)\frac{dP_0}{d\rho}\left|\tilde{\phi}\right|^2 dV \\ + \frac{c^2}{4\pi\gamma}\int\left(\frac{nq}{h}\right)^2\left(1+\zeta^2\right)\left|\frac{B_\omega}{hB_\varphi}\frac{\partial}{\partial\omega}\tilde{\phi}\right|^2 dV. \end{aligned} \tag{15}$$

4. STABILITY ANALYSIS: NUMERICAL RESULTS.

We now present numerical solutions to the stability equation (7) using a standard finite difference method with variable grid spacing. Instead of the approximate expressions (2) for the metric coefficients we use the exact ones given in the Appendix. As explained in the fundamental paper by Connor, Hastie and Taylor (1979) [6], the parameter ω_0 in the shear integral (10) must be varied and the physical solution is obtained by selecting the most unstable case. Other important parameters are the distance ρ to the separatrix, the value of the shear parameter S_o and the distance between the target plates (where the eigenfunctions have to satisfy line-tying boundary conditions) and the X-point. The effect of these parameters on the growth rates and especially on the critical β (or β^*) will be detailed below. In Figure 2 a generic case is shown for a typical set of JET-relevant parameters $\left(R_o = 1.5\text{m},\ y_o = 1.0\text{m},\ B_{t,o} = 3.0\text{T}\right)$. Shown is the growth rate of the (most unstable) fundamental mode as a function of ω_0 for three values of the parameter

$$\tilde{\beta} \equiv -\frac{4\pi}{B_{t,\,o}^2}\frac{dP_o}{d\rho}, \tag{16}$$

and using $\rho = 0.03$, while the coordinates of the end plates are $\omega_I = -\pi/4, \omega_{II} = 2\pi + \pi/4$. The normalised $\tilde{\beta}$ is connected with the usual toroidal $\beta_{tor} \equiv \frac{4\pi P_o}{B_o^2}$ by the relation

$$\beta_{tor} \approx \tilde{\beta}\frac{P}{a} \sim \left(10^{-2} - 10^{-3}\right)\tilde{\beta}.$$

The most striking aspect in Figure 2 is the strong variation of the calculated growth rate when ω_0 is near the X-point (i.e. 0 or 2π). A local minimum is reached at the outer side of the X-point (in fact, for $\tilde{\beta} = 0.0025$ the mode is stable there), and the maximum growth rate is found at a short distance (of the order of the flux coordinate ρ) *above* the X-point. Special attention is drawn to the characteristic feature that another two maxima *with exactly the same value as the first one* are present in the growth rate curve. The second one is near the outer midplane (but somewhat above it), while the third is just above the inner side of the X-point. This particular feature of the curves can easily be explained by looking at the behaviour of the shear integral (10) through the SOL. The main contribution to the integrand $\partial q/\partial\rho$ (for $S_0 = 0$) is due to the dependence of the metric coefficients on ρ:

$$\frac{\partial q}{\partial \rho}(\rho,\omega,S_0=0) \approx \frac{\partial h^2}{\partial \rho} = \frac{y_0^2}{4}\left[\frac{\exp(4\rho)+2\exp(2\rho)-3\exp(3\rho)\cos\omega}{\left(1-2\exp(\rho)\cos\omega+2\exp(2\rho)\right)^{3/2}}\right], \tag{17}$$

where we have again used the general expression for the metric coefficients (see Appendix I) rather than expansions (2) valid for $\rho<<1$.

Near the X-point we have $\cos\omega \approx 1$ and for $\omega << \rho << 1$ the numerator in the above expression is approximately equal to $-\rho$, and hence the integrand results in a negative contribution to the shear integral. For larger ω the expression changes sign. For $\omega \approx \pi/2$ for instance we obtain

$$\frac{\partial h^2}{\partial \rho} \approx \frac{3y_0^2}{8\sqrt{2}} \tag{18}$$

Because the change of sign of the integrand, and since the denominator in (17) is small near the X-point, the shear integral has the typical behaviour as depicted in Figure 3.

From Figure 3 the explanation for the three distinct points where the maximum growth rate is found in Figure 2 becomes obvious. In the stability equation (7) the parameter ω_0 only appears through the function ζ, i.e. through the shear integral. Scanning over the parameter ω_0 starting from ω_1, we encounter the first point of maximum instability, $(\omega_0)_1$. From Figure 3 it then transpires that for $\omega_0 = (\omega_0)_2$ we get

$$\int_{(\omega_0)_2}^{\omega} \frac{\partial q}{\partial \rho} d\varpi = \int_{(\omega_0)_2}^{(\omega_0)_1} \frac{\partial q}{\partial \rho} d\varpi + \int_{(\omega_0)_1}^{\omega} \frac{\partial q}{\partial \rho} d\varpi, \tag{19}$$

and since the first integral on the right hand side is identically zero, the shear integral and the *function* ζ are identical for the two values $\omega_0 = (\omega_0)_1$ and $\omega_0 = (\omega_0)_2$. Hence the stability equation is also identical for these two values, and evidently the resulting growth rates and

eigenfunctions must be identical, too. The same applies to the third maximum on the stability curve. Thus, it is clear that the reason for the ocurrence of the three identical maxima is the non-monotonic behaviour of $\partial q/\partial \rho$ as a function of ω along a flux surface in the SOL. It is to be noted that *inside* the separatrix this sort of behaviour is absent because $\partial q/\partial \rho$ is always positive there (in this analytical model). It is also clear from Figure 3 that the inclusion of the second component of the shear can substantially alter the behaviour of the shear integral for realistic values of S_0 (of the order of unity). The behaviour of the shear integral as depicted in Figure 3 is typical for the SOL in diverted plasma configurations, and is not just an artefact of this model equilibrium. To demonstrate this, we have numerically calculated (using the code GRID2D, see Simonini et al.) the metric quantities and the shear integral based on EFIT data for shot 31300 (time slice 56.1s). The resulting shear integral is shown in Figure 4. It is clear that the global shape of the curve is very similar to Figure 3 (obviously the coordinate ω is not defined the same in the two graphs). Correspondingly, the shape of the growth rate curve at fixed $\tilde{\beta}$ is similar in the experimental configuration as well (Figure 5). An important conclusion from this comparison is that the analytical equilibrium model has a very good qualitative agreement with the experiment.

An alternative, and experimentally more meaningful way of solving the stability equation (7) is to set the growth rate γ equal to zero and solve the equation for the critical (marginal) value of $\tilde{\beta}$ defining the onset of instability. In figures 6a,b the results of this calculation are presented for various values of the shear parameter S_0.

In line with the standard interpretation, the physically most relevant points on these graphs are those corresponding to the most unstable case, i.e. the *minimum* value. Obviously, the presence of the three identical maxima in figure 2 translates itself in three identical minima in the curve for $S_0 = 0$. The numerical value of $\tilde{\beta}$ at the X-point ($\omega_0 = 0$) can be compared with the analytical estimate (35). In the same scaling as used in Figure 6a, the analytical estimate becomes

$$\left(\tilde{\beta}\right)_{anal} \approx 0.012, \quad \left(\beta_{tor} \sim 10^{-4} - 10^{-5}\right) \tag{20}$$

which differs by a factor of about 3 from the numerical results. Since the analytical estimate was obtained using a constant trial function approach, the agreement is really quite good (obviously the trial function approach must necessarily overestimate the stability boundary). Also the global shape of the marginal stability curve and the influence of S_0 are represented quite well in the analytical approach.

Two further features are noteworthy in figures 6a, b: firstly, the position of minimal critical $\tilde{\beta}$ changes as S_0 is increased, and for large enough shear the minimum value is actually found *below* the X-point. Secondly, the dependence of the minimum (physical) $\tilde{\beta}_{crit}$ on S_0 is *not monotonic*. Initially, for low values, the influence of this shear component is stabilising

(compare the curves for 0 and 1), but for larger values the stability boundary is actually *lowered.*

Next we have a look at the effect of the X-point height (expressed in terms of the value of the coordinate ω at the target plates). In figure 7 we show the $\tilde{\beta}_{crit}$ curves for $S_0 = 0$ and three different positions of the target plates.

It is clear that for ω_0 above the X-point, the distance between the X-point and the target plates is rather unimportant. As expected, placing the target plates closer to the X-point does exert a stabilising influence, but unless the X-point gets very close to the target, the influence is really negligible. This feature can be explained by noting that the main effect really comes from the *total connection length between the target plates*, and at flux surfaces close to the separatrix the dominant contribution to the connection length comes from a very localized region near the X-point. It is anticipated therefore that as one goes further out into the SOL, the (stabilising) effect of the target plates becomes more important. The dependence of $\tilde{\beta}_{crit}$ on the distance to the separatrix is depicted in Figure 8 (again for $S_0 = 0$).

It is found that $\tilde{\beta}_{crit}$ is *lower* at the flux surface further out (i.e. a smaller pressure gradient would suffice to generate an instability), but one has also to take into account that the pressure is largest at the separatrix, which would favour modes localised near the separatrix to become unstable first. In figure 9 we have plotted the minimal (i.e. the physically relevant) value of $\tilde{\beta}_{crit}$ on each flux surface as a function of ρ for various values of the shear parameter S_o. All curves are of the form $c_1 + \rho c_2$ with $c_2 << c_1$. Thus, $(\tilde{\beta}_{crit})$ min is nearly constant over the SOL and the instability would therefore first appear near the separatrix where the gradients are larger.

However, finite dissipation damps the infinitely localised modes, and the most unstable mode would have some finite width (of the order of the SOL width) and be effectively driven by an average pressure gradient over this region. Therefore, to get an estimate of the toroidal plasma β required to yield instability in the SOL , we approximate

$$\frac{\partial P_o}{\partial \rho} \approx \frac{P_o}{\rho} \,. \tag{21}$$

Taking the minimal value of $\tilde{\beta}_{crit}$ for $\rho = 0.03$ in Figure 8, we obtain

$$(\beta_t)_{crit} \equiv \left(\frac{4\pi P_0}{B_{t,0}^2} \right)_{crit} \approx 3.0 \times 10^{-5}. \tag{22}$$

5. STABILITY ANALYSIS: ANALYTICAL APPROXIMATIONS

After normalisation equation (7) has the simpler form:

$$\tilde{R}\left(\frac{\partial}{\partial\omega}\right)\left(\frac{1+\zeta^2}{\tilde{R}}\right)\left(\frac{\partial}{\partial\omega}\right)\tilde{\phi}-\Gamma^2\tilde{h}^4\left(1+\zeta^2\right)\tilde{\phi}+\beta^*\tilde{h}^2\left(\frac{\partial}{\partial\rho}\tilde{R}^2-\zeta\frac{\partial}{\partial\omega}\tilde{R}^2\right)\tilde{\phi}=0, \tag{23}$$

where

$$\Gamma^2=\gamma^2\frac{q(\rho,\pi)^2R(\pi)^2}{C_A^2},\ \beta^*=-4\pi\frac{R(\pi)^2q(\rho,\pi)^2}{h(\pi)^2B_0(\pi)^2}\frac{dP_0}{d\rho}=\frac{(-4\pi)}{B_\omega(\rho,\pi)^2}\frac{dP_0}{d\rho}, \tag{24}$$

$\tilde{R}=R/R(\pi)$, $\tilde{h}=h/h(\pi)$. Here we have used the relations (11), (12) between the metric coefficients and the components of magnetic field.

We now rewrite this equation in a form that is more convenient for analytical treatment. The first derivative in (23) is eliminated by introducing the new function $u(\omega)$ defined by $\phi(\omega)=v(\omega)u(\omega)$, where $v(\omega)=1/\sqrt{\left(f/\tilde{R}\right)}$ with $f=\left(1+\zeta^2\right)$. Then the equation for $u(\omega)$ is analogous to the Schrödinger equation in quantum mechanics:

$$u''-V(\rho,\omega,\omega_0,S_0)\cdot u=0, \tag{25}$$

where the potential consists of two parts

$$V(\rho,\omega,\omega_0,S_0)=V_s(\rho,\omega,\omega_0,S_0)+\beta^*V_d(\rho,\omega,\omega_0,S_0). \tag{26}$$

The stabilising part is

$$V_s=\frac{1}{4}\left\{\ln\left(f/\tilde{R}\right)'\right\}^2+\frac{1}{2}\left[\ln\left(f/\tilde{R}\right)\right]''+\Gamma^2\tilde{h}^4, \tag{27}$$

and the destabilising one is

$$V_d=-\left(\tilde{h}^2/f\right)\left(\frac{\partial}{\partial\rho}\tilde{R}^2-\zeta\frac{\partial}{\partial\omega}\tilde{R}^2\right). \tag{28}$$

The typical dependence of V_s and V_d on ω is plotted in figure 10. The potential is obviously strongly localised near the X-point.

Equation (23) has been solved numerically in the previous section. Here we present analytical results that can be derived if the strong localisation of the potential $V(\omega)$ near the X-point is taken into account. Then the simplified expressions (5), (6) for the metric

coefficients near the X-point can be used. In the variable $t = \omega/\rho$ the differential equation assumes the form:

$$\frac{\partial}{\partial t}\left(1+t^2\right)\frac{\partial}{\partial t}\tilde{\phi} - 4\,\Gamma^2\tilde{\phi} + \hat{\beta}\frac{\left[t+\left(1+t^2\right)^{1/2}\right]^{1/2}}{\left(1+t^2\right)^{1/2}}\tilde{\phi} = 0. \tag{29}$$

Here a new dimensionless beta is defined

$$\hat{\beta} = \frac{\sqrt{2}y_0}{R(\pi)}\rho^{1/2}\beta^* = -2^{5/2}\pi\ \frac{y_o}{R(\pi)}\rho^{1/2}\ \frac{1}{B_\omega(\rho,\pi)^2}\ \frac{dP_o}{d\rho} \tag{30}$$

For the new function u(t):

$$\tilde{\phi}(t) = \frac{1}{\sqrt{1+t^2}}u(t), \tag{31}$$

the equation:

$$u''_{tt} - V(t)u = 0, \tag{32}$$

is obtained with $V(t) = V_s(t) + \hat{\beta}\cdot V_d(t)$, where

$$V_s(t) = \left(\frac{4\Gamma^2}{\left(1+t^2\right)} + \frac{1}{\left(1+t^2\right)^2}\right),\ V_d(t) = -\left(\frac{\left[1+\left(1+t^2\right)^{1/2}\right]^{1/2}}{\left(1+t^2\right)^{3/2}}\right) \tag{33}$$

and $\Gamma^2 = \dfrac{\gamma^2 q(\rho,\pi)^2 R(\pi)^2}{C_A^2}$ is the normalised growth rate.

Equation (32) can be derived from the variational form (13) which assumes now a simpler form:

$$E = \frac{1}{2}\int_{-\infty}^{+\infty}\left[\left(u'_t\right)^2 + V(t)\cdot u^2\right]dt. \tag{34}$$

Here we can extend the limits of integration up to infinity as V(t) falls off sufficiently fast for $|t|\to\infty$.

The variational form is convenient to estimate growth rates and, in particular, to get a marginal stability criterion. Choosing as trial function $u(t) = c_1$, where c_1 is constant, and setting $\Gamma = 0$ we find the marginal stability condition.

$$\int_{-\infty}^{+\infty} V(t)\,dt = 0$$

The threshold beta that follows from this condition is:

$$\hat{\beta}_{cr} = -\frac{\int_{-\infty}^{\infty} V_s(t)dt}{\int_{-\infty}^{\infty} V_s(t)dt} = \frac{\int_{-\infty}^{\infty} \left(1+t^2\right)^{-2} dt}{\int_{-\infty}^{\infty} \left[1+\left(1+t^2\right)^{1/2}\right]^{1/2} \left(1+t^2\right)^{-3/2} dt} = 0.5. \tag{35}$$

Note that in terms of the parameter $\tilde{\beta}$ this corresponds to a scaling $\tilde{\beta} \propto \rho^{-1/2}$. This scaling is verified in Figure 11. We can rewrite the resulting *sufficient* condition for instability $\hat{\beta} > \hat{\beta}_{cr}$ in terms of the plasma parameters at the midplane:

$$\frac{q(\pi)^2 4\pi P_0}{B_0(\pi)^2} > \frac{1}{2^{3/2}} \frac{y_0}{R(\pi)} \left(\frac{(\Delta x)_0}{y_0}\right)^{1/2} \propto \frac{b}{R_0} \left(\frac{(\Delta x)_0}{b}\right)^{1/2}. \tag{36}$$

Here we assume as in Eq. (4) that y_0 corresponds to the vertical semi-axis, i.e. $y_0 \sim b$, and estimate $\frac{dP_0}{d\rho}$ as $\frac{P_0}{\Delta\rho}$, where $\Delta\rho \approx (\Delta x)_0 / y_0$ and $(\Delta x)_0$ is the pressure gradient length scale at the separatrix at the midplane (according to present-day L-H threshold theories $(\Delta x)_0$ can be of the order of a few Larmor radii), and $B_0(\pi)$ is the toroidal magnetic field on the magnetic axis. The safety factor $q(\pi) \equiv q(\rho, \pi)$ near the separatrix is related to the usual q inside the separatrix $q(\rho) = \delta\Phi(\rho)/\delta\psi(\rho)$, where Φ and ψ are the toroidal and poloidal fluxes respectively, by the relation:

$$q(\rho) = q(\pi)\Lambda, \tag{37}$$

where

$$\Lambda = (2/\pi) \cdot \ln(4\pi/\rho) \tag{38}$$

takes the usual divergence of q near the separatrix into account. The widely used quantity $q_{95} = q(\rho = -0.05)$ is for our model related to $q(\pi)$ by:

$$q_{0.95} \approx 3 \cdot q(\pi). \tag{39}$$

It is interesting to compare the result (36) with the result derived in the slab model for the SOL [10]:

$$\frac{q^2 4\pi P_0}{B_0^2} > \frac{(\Delta x)_0 R q^2}{L_{\parallel}^2} \propto \frac{(\Delta x)_0}{R}, \tag{40}$$

Here $L_{||}$ is the connection length - the distance between the end plates along the magnetic field line (see Appendix I). We assume that $L_{||} \propto qR$.

The resemblance becomes more transparent and the physical meaning of the criterion (36) clearer when we rewrite (36) in terms of the pressure gradient near the X-point rather than at the midplane [10]:

$$\frac{q(\pi)^2 4\pi P_0}{B_0^2(\pi)^2} >\approx \frac{y_0}{R(\pi)}\left(\frac{(\Delta x)_0}{y_0}\right)^{1/2} \propto \frac{(\Delta x)_x}{R_0} \tag{41}$$

where $(\Delta x)_x \approx \left((\Delta x)_0 y_0\right)^{1/2}$. The similarity between (40) and (41) is obvious. The result (41) denotes that the main effect comes from the plasma in a tube with radius of the order $\rho \approx (\Delta x)_x$ and length $L \approx qR$ located near the X-point.

In Fig. 12 a typical eigenfunction for ϕ is shown. Physical quantities like plasma displacement and the perturbation of the transverse magnetic field are proportional to the first and second derivatives of the potential ϕ and are more localised near the X-point, as illustrated in Fig. 13.

It is easily seen that the metric (2) can also be applied inside the separatrix, defined by $\rho < 0$. However, it should be kept in mind that inside the separatrix the magnetic well has to be included in the stability calculations. This well generates an additional stabilising influence.

We conclude this section by addressing the relation of Mercier's criterion to the ballooning type criterion (36). It is well known that Mercier's criterion is related to the behaviour of the differential equation (23) and its solutions for $\omega \rightarrow \pm\infty$ (see for example the review [11]). For the region outside the separatrix the coordinate is confined to a finite domain, so that the asymptotic properties of the differential equation do not appear. Therefore, Mercier's criterion is not relevant for the SOL calculations.

6. ELMS AS EDGE MODES

The physical effects which can be a consequence of the nonlinear development of the interchange modes are now discussed [12]. We first summarise our physical picture of the processes involved. Initially, the instability starts near the X-point as derived above. From the linear stability theory the main parameters of these MHD perturbations are established, which allows us to draw some conclusions on the nonlinear evolution. The perturbations have a width of order ρ and an extended tail as determined from the eigenfunction. The structure in the coordinate ρ can be estimated from the metric Eq. (2). Denoting the characteristic scale length for the pressure gradient at the midplane as $(\Delta x)_0$, the gradient length near the X-point is given by:

$$(\Delta x)_x = \left((\Delta x)_0 y_0\right)^{1/2}, \tag{42}$$

where $y_0 \sim b$. During the MHD phase the plasma in the tube with a radius given by (42) near the X-point is removed and lost onto the target plates. The energy which is lost during this event is of the order:

$$\Delta W_x \approx \pi\left[(\Delta x)_x\right]^2 P_{edge} \cdot 2\pi R \tag{43}$$

where P_{edge} is the plasma pressure at the separatrix. From (43) we can estimate the relative energy loss:

$$\delta_x = \frac{\Delta W_x}{W} \approx \frac{\pi(\Delta x)_x^2}{\pi ab} \frac{P_{edge}}{\bar{P}_0} \tag{44}$$

Here $W = 2\pi^2 a \cdot b \cdot R\bar{P}_0$ is the total energy content, when the area of the plasma cross section is approximately πab, and $\bar{P}_0$ is the average plasma pressure.

If we choose $(\Delta x)_x \sim 15$cm, a ~ 100cm, b ~ 200cm, and $P_{edge}/\bar{P}_0 \sim 0.2$ then $\delta_X \sim 0.2\%$. This value is too small to account for the energy lost during a giant ELM, i.e. the interchange instability near the X-point can only be considered as some precursor event. This can explain the experimental result that ELMs initially appear preferentially near the X-point. When the perturbations near the X-point become sufficiently large they can trigger the interchange instability in the main plasma.

The scenario can be as follows. After the instability appears near the X-point it expels plasma from this region and destroys the separatrix locally; it is well known that the separatrix distortions are largest near the X-point. Both these processes yield a strong plasma interaction with the end plates or the side wall. This interaction produces a cold `dirty' plasma with low conductivity that fills the region near the X-point. This is the first stage of the process. This new plasma plays the role of 'an effective limiter', which is placed inside the separatrix. Due to the low conductivity the field lines are no longer frozen to the plasma near the X-point. The MHD perturbations inside the separatrix have `unfrozen' boundary conditions and the main plasma near the separatrix becomes MHD unstable to the usual flute perturbations. This is the second stage of the process and the mechanism for the appearance of the giant ELMs. In the third stage there is refilling of the empty region by hot plasma from the centre on the diffusive time scale [13].

The core plasma interchange instabilities can release much more energy than those localised near the separatrix. They are macroscopic and for this reason the separatrix effects do not play an important role. Therefore we can consider the region inside the separatrix with width a/nq (see below) in the usual quasi-cylindrical approximation. Then the perturbations at

the plasma surface comprise a plasma tube with a width of order a/m (the most unstable mode have m~nq) and length qR. These perturbations have an effective radial width $\Delta a \approx a/(nq)$ and a global poloidal extent. A plasma layer with width Δa near the boundary is removed during the nonlinear stage of the global instability. This gives the following estimate for the lost energy:

$$\Delta W \approx \pi ab \frac{P_{edge}}{(nq)} \cdot 2\pi R \tag{45}$$

From (45) we can estimate the relative energy loss for the global interchange instability:

$$\delta = \frac{\Delta W}{W} \approx \frac{P_{0edge}}{(nq)\bar{P}_0} \tag{46}$$

For $n \sim 1$, $q \sim 5$ and $P_{0edge}/\bar{P}_0 \sim 0.2$ this yields $\delta \approx 4\%$.

The time to restore the lost energy (45) due to heating is:

$$\frac{1}{\tau} = \frac{P}{\Delta W} \tag{47}$$

where P is the heating power. The time (47) is the ELM repetition time. Combining (45) and (47) we find:

$$\tau \approx \frac{\pi ab P_{0edge}}{(nq)P} \approx \frac{1}{nq}\frac{W}{P}\frac{P_{0edge}}{\bar{P}_0} \tag{48}$$

As a very approximate estimate for (48) we can write:

$$\tau = \frac{1}{nq}\tau_E \frac{P_{0edge}}{\bar{P}_0}, \tag{49}$$

where $\tau_E \approx W/P$ is the energy confinement time. For $n \sim 1$, $q \sim 5$ and $P_{0edge}/\bar{P}_0 \sim 0.2$ one has $\tau \approx 4x10^{-2}\tau_E \sim 4-20$ msec.

We can rewrite the result (48) in a more physical way by introducing the plasma current I [12]:

$$f = \frac{1}{\tau} \propto nq\frac{P}{W} \propto \frac{PB_0}{I^3(\Delta x)_0^{1/2}} \tag{50}$$

where $(\Delta x)_0$ is the pressure gradient length scale on the separatrix at the mid-plane. From this result it follows that the ELM frequency scales linearly with the applied heating power, but stronger than inversely with the total current. Details of the scrape-off-layer contribute through the width $(\Delta x)_0$. However, this dependence is weak.

The theoretical scaling (50) for the ELM frequency is compared with the experimental data in figure 14 where the theoretically predicted linear dependence of the giant ELM frequency on heating power can be clearly recognised. In the relations (47) and (50) P denotes the net heating power, taking into account power losses by e.g. radiation. In Figure 14 the total input power is used as the ordinate, i.e. losses are not accounted for. It is found that the experimental results can be well fitted by subtracting 1.5 MW as losses from the total heating power.

In these JET discharges q_{95}, the value of the safety factor near the separatrix which defines the width of the surface mode through nq in equation (50), is nearly constant. Thus, an inverse quadratic dependence for given heating power and magnetic field is predicted with only a weak dependence on the pressure gradient length Δx_0, i.e.

$$f \propto \frac{P - P_r\, B_0}{I^2 (\Delta x)_o^{1/2}} \tag{50a}$$

This inverse quadratic scaling with current is also well reproduced by the three curves in Figure 14.

7. CONCLUSIONS.

The basic result is that the presence of a separatrix changes qualitatively the condition for the existence of interchange MHD instabilities. For plasmas with a separatrix the edge perturbations are localised mainly near the X-point. The threshold beta for perturbations occurring just outside the separatrix has been computed by solving Eq. (7) numerically for JET discharges as well as for model equilibria. It has been established that the simplified analytic metric Eq. (2) is reasonably accurate. The analytically derived critical beta for marginal stability (36) agrees well with the numerical solution. MHD interchange type pertubations in the SOL can become unstable more easily than the corresponding internal perturbations, which experience the stabilising effect of the magnetic well.

It is found that the critical beta behaves as $\tilde{\beta}_{cr} = C_1 - \rho C_2$ with C_1, $C_2 > 0$ and $C_2 << C_1$ with respect to the distance from the separatrix. The transition zone from closed to open field lines is typically one to several poloidal gyroradii wide and, consequently, the pressure gradient is largest there. Outside this transition region the pressure is found experimentally to fall off exponentially. This implies that the flux surface, where the ballooning criterion is violated first, is very close to the separatrix. The lower threshold further out is compensated by a faster pressure decay. However, it is also physically evident that the ballooning criterion needs to be violated over a small region outside the separatrix and the resulting perturbation is given by the envelope.

It is important to note that these perturbations can remove only a small part of the total stored energy but they do destroy the magnetic separatrix near the X-point. These effects lead to

a filling of the X-point region by cold and high-Z plasma due to the interaction with the end plates or the wall of the chamber. This cold plasma with low conductivity acts like effective target plates for the plasma tube with width of order $\Delta a \approx a/(nq)$ inside the separatrix. It destabilises the interchange instability of the main plasma.

From this scenario we can estimate the frequency of ELMs (50) and its dependence on the heating power and on the plasma current. At modest heating power the ELM frequency is found to decrease with P supporting the idea of stabilisation of dissipative (e.g. resistive interchange) instabilities. The giant ELMs, in contrast, appear as a hard, i.e. ideal MHD, limit. Their repetition rate scales linearly with power, as is confirmed by the experimental results displayed in fig 14. The explanation as an ideal beta limit yields the scaling of $f \alpha I/I^2$ when q_{95} (which determines the mode width Δa) is kept constant, otherwise the scaling is $f \alpha I/I^3$.

The evolution of the giant ELM consists of three steps: firstly the appearance of an interchange instablility near the X-point causing the influx of cold high-Z plasma on a characteristic time scale τ_1, secondly the trigger of the major interchange instability on a fast time scale τ_2 and, thirdly, the refilling of the removed plasma layer inside the separatrix by hot plasma from the centre on the diffusion time scale τ_3 [13]. Reasonable correlation between the theoretical predictions and the experimental results is found.

APPENDIX 1. METRIC FOR SEPARATRIX GEOMETRY

It is well known that in cylindrical geometry any harmonic function Φ of the complex argument $Z = x + iy$ satisfies the vacuum magnetic field equation $\Delta\Phi = 0$. Therefore, this concept is used for the derivation of orthogonal flux coordinates for straight cylindrical geometry but allowing for a plasma shape with a separatrix. This two-dimensional solution is then combined with the toroidal angle φ, in order to provide a suitable approximation to a realistic tokamak geometry close to the separatrix. The complex function $W = \psi + i\omega$ is introduced:

$$W=\ln Z1+\ln Z2=\ln(Z1Z2) \tag{A1.1}$$

Here ln(Z1), ln(Z2) are the flux functions for the straight current strings, which are placed at points with the coordinates $(0, y_0)$ and $(0, -y_0)$, and $Z1=x+i(y-y_0)$, $Z2=x+i(y+y_0)$. Separating the real and imaginary parts in (A1.1) we find:

$$\begin{aligned} \exp(\psi)\cdot\cos(\omega) &= x^2 - y^2 + y_0^2 \\ \exp(\psi)\cdot\sin(\omega) &= 2xy. \end{aligned} \tag{A1.2}$$

For the separatrix it holds that $\psi_s = \ln\left(y_0^2\right)$. In the SOL $\psi > \psi_s$ and ω varies between ω_I and ω_{II}, in the plasma inside the separatrix $\psi < \psi_s$ and ω varies between 0 and 2π. Rewriting the length element $(ds)^2=(dx)^2+(dy)^2$ in the new coordinates (ψ,ω) we obtain:

$$(ds)^2 = \frac{1}{4}\frac{\exp(2\psi)}{4\left[y_0^4 - 2y_0^2\exp(\psi)\cos(\omega) + \exp(2\psi)\right]^{1/2}}\left[(d\psi)^2 + (d\omega)^2\right] \tag{A1.3}$$

We replace ψ by the new coordinate ρ, which describes the distance from the separatrix: $\rho = \psi - \psi_s$. In the SOL $\rho > 0$, and inside the separatrix $\rho < 0$. Near the separatrix $|\rho| << 1$ we can simplify the metric (A1.3) and choose the following model for the toroidal metric near the separatrix:

$$(ds)^2 = h_\rho^2(d\rho)^2 + h_\omega^2(d\omega)^2 + R^2(d\varphi)^2, \tag{A1.4}$$

where the metric coefficients h_ρ and h_ω are deduced from (A1.3):

$$h_\rho = h_\omega = h, \tag{A1.5}$$

$$h^2 = \frac{y_0^2}{2^{5/2}}\frac{1}{\left[1-\cos(\omega)+\rho^2/2\right]^{1/2}}. \tag{A1.6}$$

This metric is suitable for the description of the SOL plasma and has to be corrected for the plasma inside the separatrix as it does for example not take the magnetic well into account.

From the equations $\mathrm{rot}\vec{B} = 0$ and $\mathrm{div}\vec{B} = 0$ we can derive the components of the magnetic field (11), (12) together with the geometrical parameters. The normalised $\tilde{h}$ is approximated by:

$$\tilde{h}(\rho,\omega) = h(\rho,\omega)/h(\pi) \cong \frac{2^{1/4}}{\left[1-\cos(\omega)+\rho^2/2\right]^{1/4}}, \tag{A1.7}$$

where

$$h(\pi) = \frac{y_0}{2^{5/4}} \frac{1}{\left[2+\rho^2/2\right]^{1/4}} \cong \frac{y_0}{2^{3/2}}; \tag{A1.8}$$

the safety factor is:

$$q(\rho,\omega) = \frac{h_\omega B_0}{R B_\omega} \cong q(\rho,\pi) \frac{\left(\tilde{h}(\rho,\omega)\right)^2}{\tilde{R}}, \tag{A1.9}$$

where

$$q(\rho,\pi) = \frac{h(\pi)B_0(\pi)}{R(\pi)B_\omega(\rho,\pi)}. \tag{A1.10}$$

Near the separatrix this quantity depends very weakly on ρ and the main dependence of q on ρ appears due to $\tilde{h}(\rho,\omega)$ in (A1.9). The quantity (A1.10) is connected with the more familiar quantity q_{95} by relation (39).

The connection length is $L_{||}$ is $L_{||}(\rho) = l_{||}(\rho,\omega_{II},\omega_I)$, where $l_{||}(\rho,\omega,\omega_I)$ is the distance along the magnetic field line from the outer end plate.

$$l_{||}(\rho,\omega,\omega_I) = R(\pi)q(\rho,\pi)\int_{\omega_I}^{\omega} h^{-2}d\omega. \tag{A1.11}$$

The coordinate ω can be replaced by the poloidal length along a poloidal cross-section of a flux surface.

$$l(\rho,\omega,\omega_I) = \int_{\omega_I}^{\omega} h_\omega d\omega. \tag{A1.12}$$

The dependencies $\ell_{||}(\rho,\omega,\omega_I)$ and $\ell(\rho,\omega,\omega_I)$ for $\omega_I = -\pi/5$ are plotted in figures 15a,b. From these figures it is clear that the major contribution to the field line length originates from the X-point region.

The expression (10), which reflects the influence of the magnetic shear, can be split into two parts:

$$\zeta(\rho,\omega,\omega_0,S_0)\approx\left(\frac{S_0}{\tilde{h}(\rho,\omega)^2}\int_{\omega_0}^{\omega}\tilde{h}(\rho,t)^2dt+\frac{1}{\tilde{h}(\rho,\omega)^2}\frac{\partial}{\partial\rho}\int_{\omega_0}^{\omega}\tilde{h}(\rho,t)^2dt\right) \qquad (A1.13)$$

where in the first term

$$S_0=\frac{1}{q(\rho,\pi)}\frac{\partial}{\partial\rho}q(\rho,\pi) \qquad (A1.14)$$

is the shear related to the plasma current and the second term in (A1.13) is connected with the presence of the separatrix. Typically S_0 is of order unity. Far from the separatrix, where the dependence of the metric coefficients on the poloidal coordinate ω becomes weak, the first term in (A1.13) has the usual form ωS_0 and the second one is unessential. Near the separatrix both terms are of comparable value (for $S_0\approx 1$).

APPENDIX 2

Let us consider in more detail the stability equation for the case of small ρ,ω. In this limit we can write:

$$\tilde{x}(\rho,\omega) \approx \frac{y_o}{R_o\sqrt{2}}\left[\rho+\left(\rho^2+\omega^2\right)^{1/2}\right]^{1/2}\mathrm{sgn}(\omega). \tag{A2.1}$$

Where $\mathrm{sgn}(\omega)$ needs to be taken into account only inside the separatrix $(\rho<0)$. Outside $(\rho>0)$ it has to be omitted. Then the curvature terms can be expressed as:

$$\frac{\partial\tilde{x}}{\partial\rho}=\tilde{x}_\rho=\frac{y_o}{R_o 2^{3/2}}\frac{1+\rho/\left(\rho^2+\omega^2\right)^{1/2}}{\left[\rho+\left(\rho^2+\omega^2\right)^{1/2}\right]^{1/2}}\mathrm{sgn}(\omega) \tag{A2.2}$$

and

$$\frac{\partial\tilde{x}}{\partial\omega}=\tilde{x}_\omega=\frac{y_o}{R_o 2^{3/2}}\frac{\omega/\left(\rho^2+\omega^2\right)^{1/2}}{\left[\rho+\left(\rho^2+\omega^2\right)^{1/2}\right]^{1/2}}\mathrm{sgn}(\omega). \tag{A2.3}$$

For simplicity we only consider the case $\omega_0=0=S_0$. The shear term for small ρ,ω then has the form:

$$\zeta(\rho,\omega)\approx-\omega/\rho. \tag{A2.4}$$

and

$$f(\rho,\omega)\equiv 1+\zeta^2\approx 1+(\omega/\rho)^2 \tag{A2.5}$$

The stabilising part $V_s(\rho,\omega)$ of the potential $V(\rho,\omega)=V_s(\rho,\omega)+\beta^*\cdot V_d(\rho,\omega)$ becomes:

$$V_s(\rho,\omega)\approx\frac{1}{\left(1+t^2\right)^2}, \tag{A2.6}$$

where $t=\omega/\rho$, and

$$V_d(\rho,\omega)=-2\frac{\rho^2\tilde{h}^2}{\left(1+\zeta^2\right)}\left(\frac{\partial\tilde{x}}{\partial\rho}-\zeta\frac{\partial\tilde{x}}{\partial\omega}\right)\approx\sqrt{2}\,\frac{y_o}{R(\pi)}\frac{|\rho|^{1/2}}{\left(1+t^2\right)^{3/2}}\left[\left(1+t^2\right)^{1/2}-1\right]^{1/2}\mathrm{sgn}(\omega), \tag{A2.7}$$

for $\rho<0$ and

$$V_d(\rho,\omega) = -2\frac{\rho^2\bar{h}^2}{\left(1+\zeta^2\right)}\left(\frac{\partial\tilde{x}}{\partial\rho} - \zeta\frac{\partial\tilde{x}}{\partial\omega}\right) \approx -\sqrt{2}\,\frac{y_o}{R(\pi)}\frac{\rho^{1/2}}{\left(1+t^2\right)^{3/2}}\left[\left(1+t^2\right)^{1/2}+1\right]^{1/2}, \qquad \text{(A2.8)}$$

for $\rho > 0$.

REFERENCES

1. The H-mode of ASDEX, ASDEX Team, Nucl. Fusion 29 (1989), p.1959.
2. W. Kerner et al., Bull. Am. Phys. Soc. 36 (1991) 2R13, p. 2310.
3. H.J. Doyle et al 1991 Proc. 18th Europian Conf. on Control. Fusion and Plasma Physics (Berlin 1991) Vol 1 (Vienna: IAEA) p. 285.
4. H.J. de Blank, M.F.F. Nave, W. Kerner, G.T.A. Huysmans, Resistive Ballooning Analysis for Edge Localized Modes in JET Discharges, JET-P(93)23.
5. J.G. Cordey, W. Kerner and O. Pogutse, Plasma Phys, and Contr. Fusion 37 (1995), 773.
6. J. Connor, R. Hastie and B. Taylor, Proc. R. Soc. (London), Ser. A 365 (1979) 1.
7 C.M. Bishop, P. Kirby, J.W. Connor, R.J. Hastie, J.B. Taylor, Nuclear Fusion 24 (1984) 1579.
8. C.M. Bishop, Nuclear Fusion 26, (1986) 1063.
9. O.P. Pogutse and E.I. Yurchenko, Nuclear Fusion 18 (1629) 1978.
10. W. Kerner and O. Pogutse, in Proceedings of 21st EPS Conference Controlled Fusion and Plasma Physics, Montpellier, 1994), vol II, p.882.
11. O. Pogutse and E. Yurchenko, Review of Plasma Physics, Consult Bureau, New York - London, Vol. 11 (1986), p.65
12. O. Pogutse, J.C. Cordey, W. Kerner, Proc. 22nd EPS Conf. on Controlled Fusion and Plasma Physics (Bournemouth, 1995), Vol III p. 277.
13. V.V. Parail et al, 15th IAEA Conf. on Plasma Phys. and Cont. Fusion Res., (Seville, 1994), IAEA-CN-60/A-2-II-3.

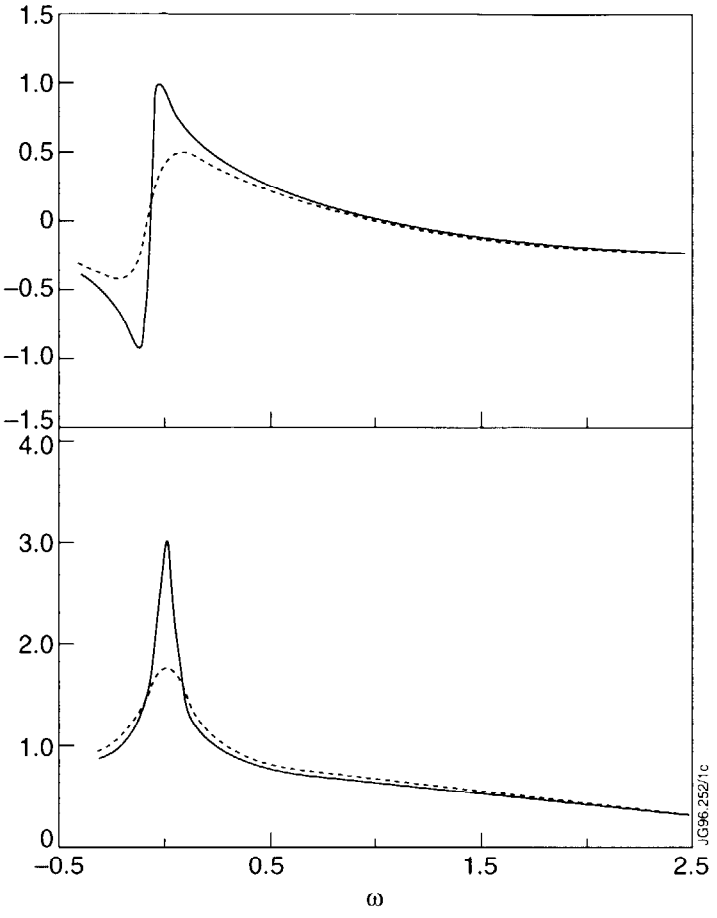

Fig 1: The derivatives $\frac{\partial x}{\partial \rho}$ *(bottom) and* $\frac{\partial x}{\partial \omega}$ *(top) as a function of* ω*, for* $\rho = 0.03$ *(full curve) and* $\rho = 0.1$ *(dashed curve).*

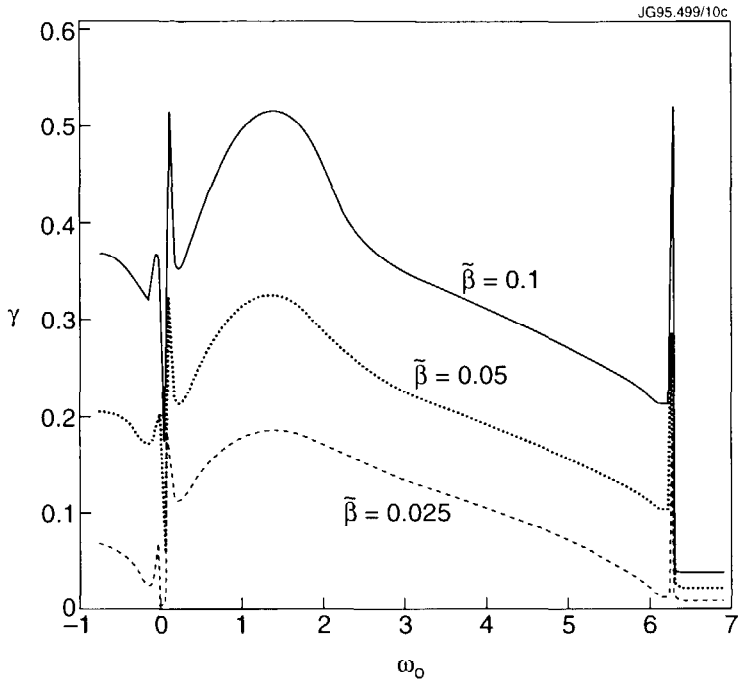

Fig.2: Growth rate of the fundamental mode as a function of the eikonal quasi-mode origin ω_0 *at the flux surface given by* $\rho = 0.03$. *The three curves are for* $\tilde{\beta} \approx 0.01, 0.005, 0.0025$ *(top to bottom). The divertor target plates were positioned at a distance* $\pi/4$ *below the X-point. Other parameters for the equilibrium are* $S_0 = 0$, $R_0 = 1.5\text{m}$, $y_0 = 1.0\text{m}$, $B_{t,0} = 3.0\text{T}$, $B_{\omega,0}(\rho, \omega = \pi) = 0.1\left(R_0 h(\rho, \pi)\right)^{-1}\text{T}$.

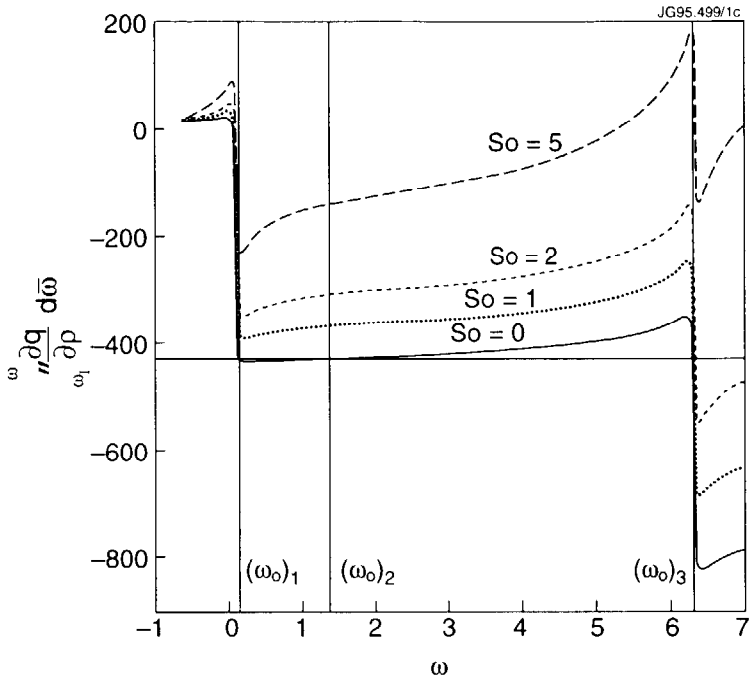

Fig.3: The shear integral $\int_{\omega_1}^{\omega} \frac{\partial q}{\partial \rho} d\varpi$ *for the equilibrium parameters used in figure 2 (full curve) and for* $S_0 = 1$, *2 and 5 (dashed curves). The three points where the maximum growth rate is obtained for* $S_0 = 0$ *are indicated by vertical lines.*

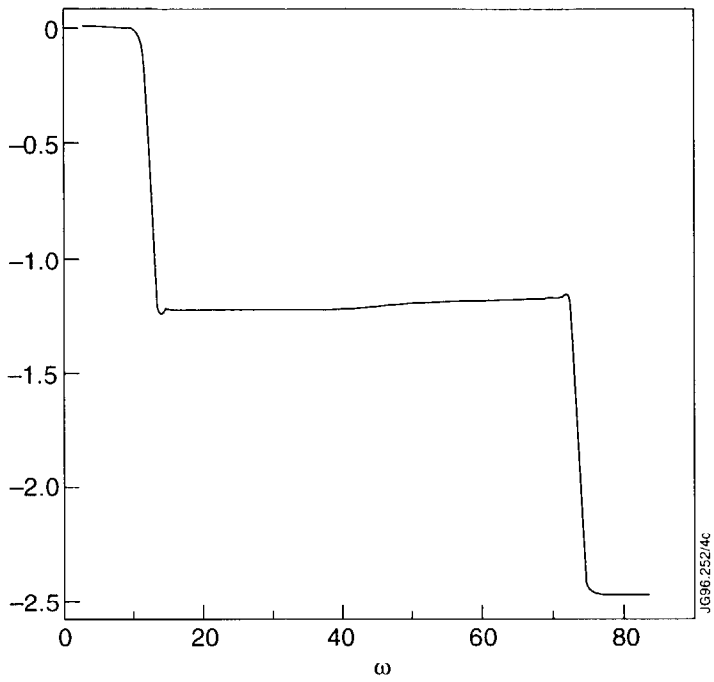

Fig.4: The shear integral $\int_{\omega_1}^{\omega} \frac{\partial q}{\partial \rho} d\varpi$ *calculated at a flux surface a few millimeters away from the separatrix in the SOL, for a JET experimental magnetic configuration (shot 31300 at time 56.1). The metric quantities were calculated using the GRID2D code (Simonini et al.), based on the magnetic equilibrium reconstruction with EFIT.*

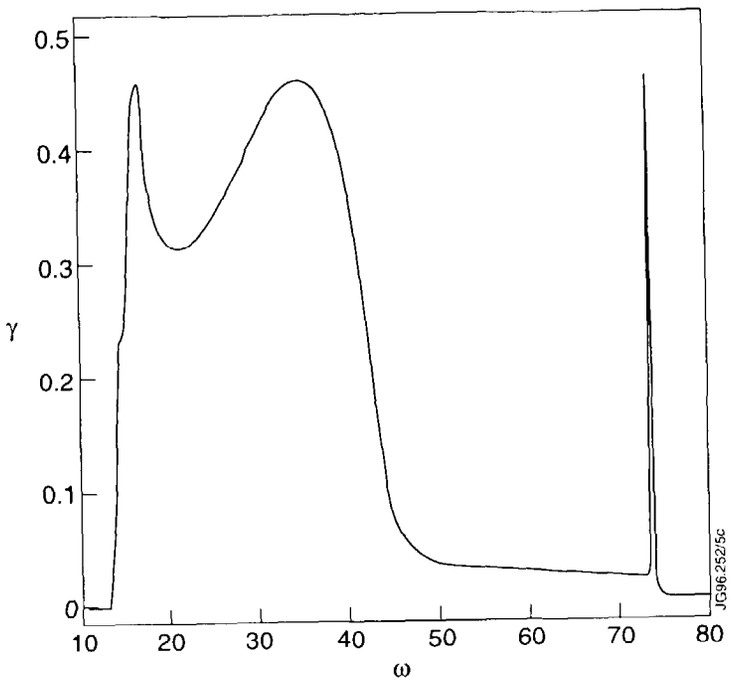

Fig. 5: The growth rate as a function of ω_0 *for the same case used in Figure 4, and with* $\bar{\beta} = 0.001$.

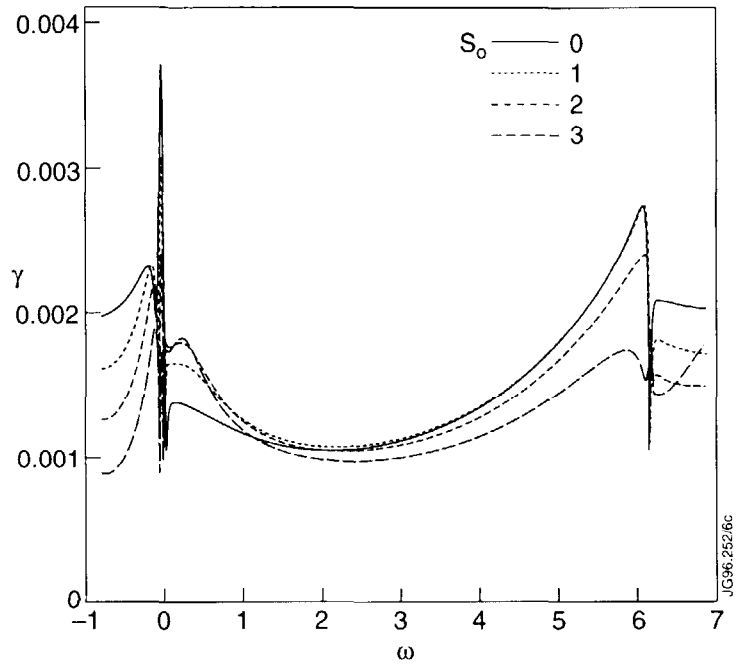

Fig. 6a: Critical (marginal) value of $\tilde{\beta}$ *as a function of* ω_0 *for different values of the shear parameter* S_0. *The other equilibrium parameters are as in Figure 2.*

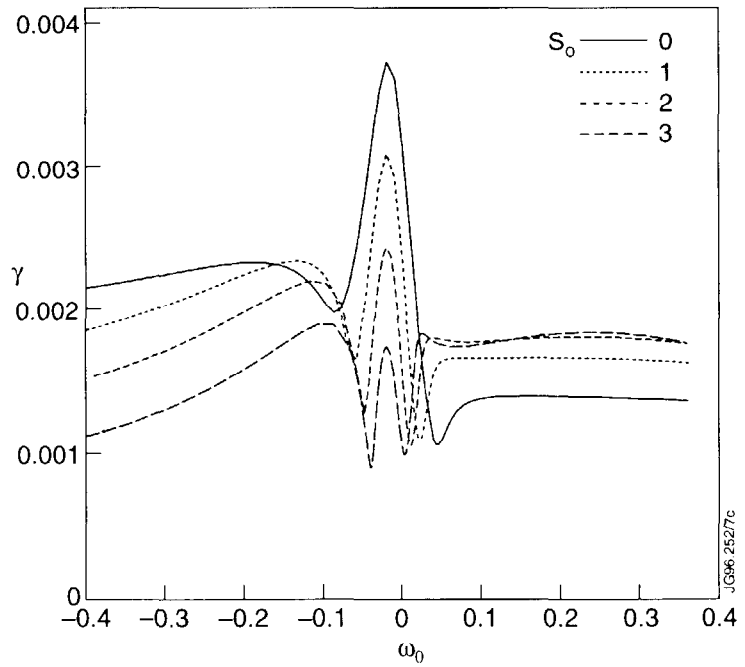

Fig. 6b: An enlargement of the region near the outer side of the X-point in Figure 6a.

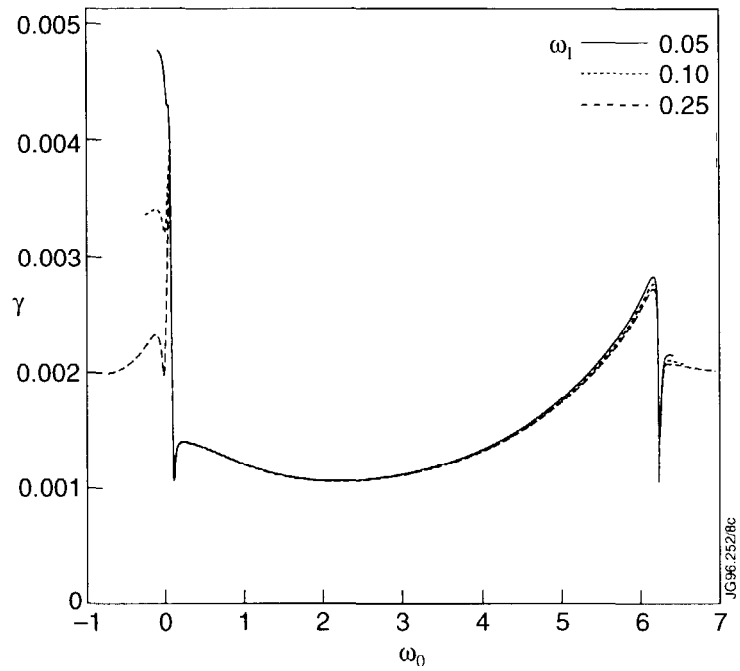

Fig. 7: Critical value of $\tilde{\beta}$ *as a function of* ω_0 *for target plates at 'distances' (in the coordinate* ω*) of* 0.25π, 0.1π, *and* 0.05π *below the X-point. Other equilibrium parameters are as in Figure 2.*

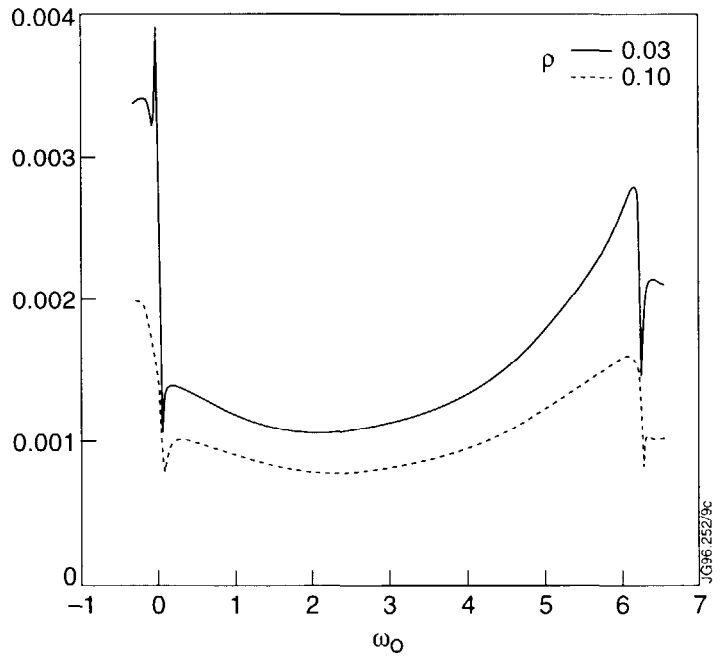

Fig. 8: Critical value of $\tilde{\beta}$ *as a function of* ω_0 *at two flux surfaces,* $\rho = 0.03$ *and* $\rho = 0.1$, *with target plates* 0.1π *below the X-point. Other equilibrium parameters are as in Figure 2.*

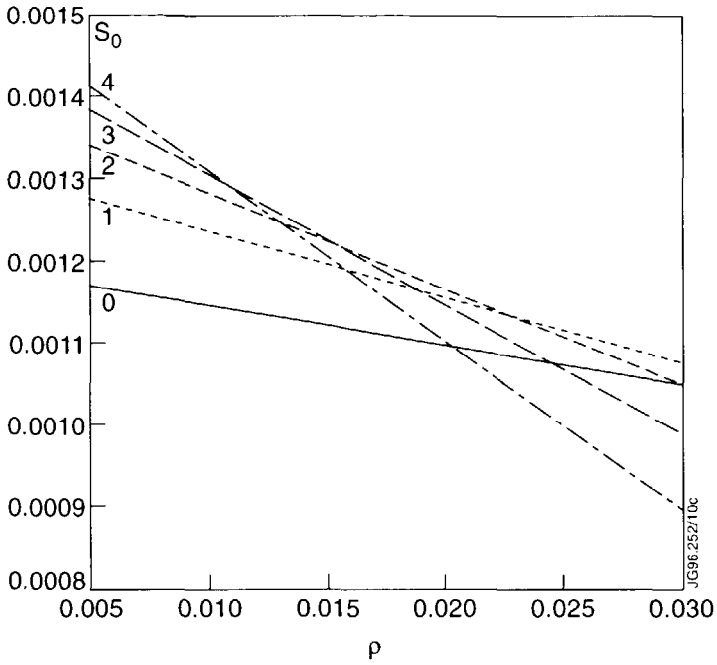

Fig. 9: The minimal value of $\bar{\beta}_{crit}$ *on each flux surface as a function of* ρ *for* $S_O = 0, 1, 2, 3$ *and 4. Other parameters are as in Figure 8.*

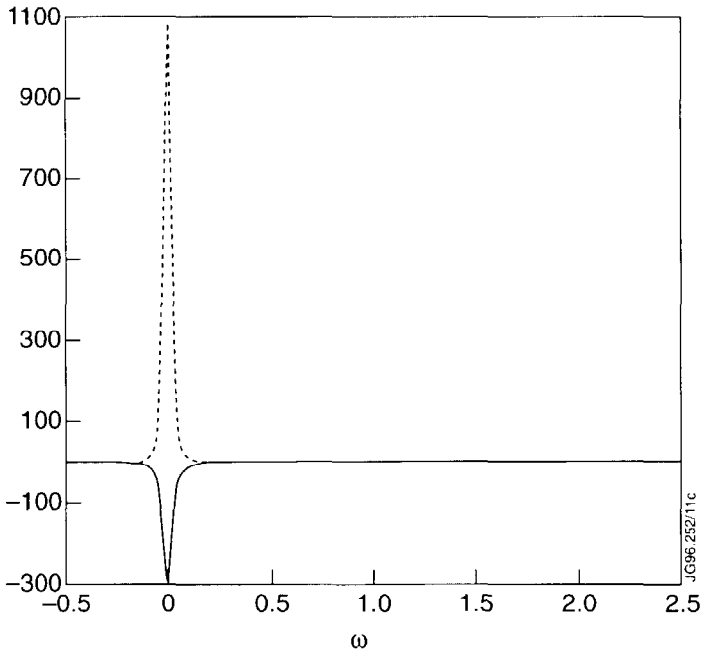

Fig. 10: Typical behaviour of the potentials V_S *(dashed curve) and* V_d *(full curve) defined in eq. (27), (28), for* $\omega_O = S_O = \Gamma = 0$ *and* $\rho = 0.03$.

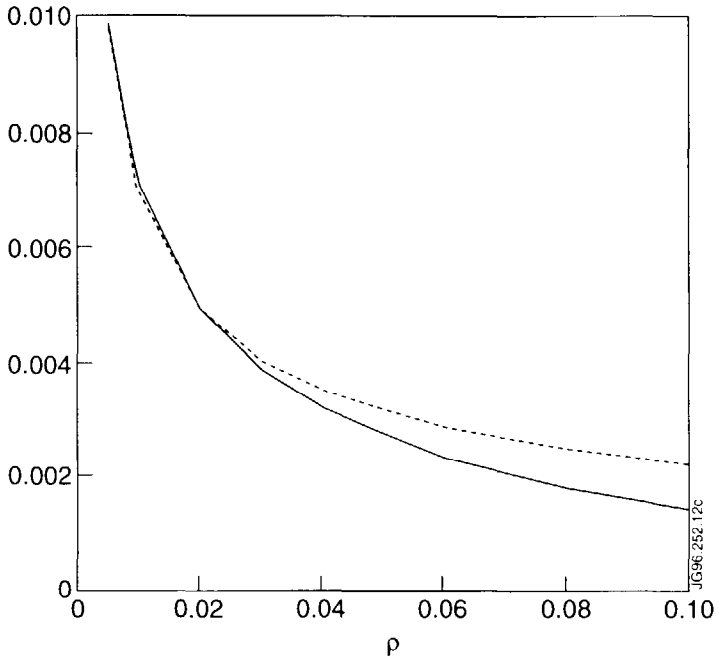

Fig. 11: The numerically calculated $\tilde{\beta}_{crit}$ *for* $\omega_0 \equiv 0$ *and* $S_0 \equiv 0$ *as a function of* ρ *(full curve). The dashed curve gives a* $\rho^{-1/2}$ *dependence assuming identical values at the smallest r.*

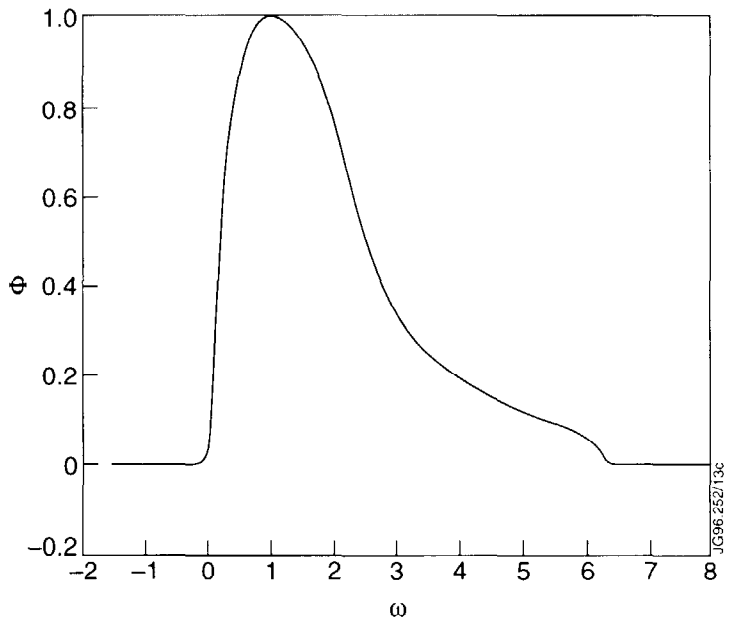

Fig. 12: Typical eigenfunction for ϕ *as obtained from the numerical solution of eq. (7), for* $\rho = 0.03$, $S_0 = 0$, $\omega_I = -\frac{\pi}{2}$ *and* ω_0 *selected to give the minimum* $\tilde{\beta}_{crit}$.

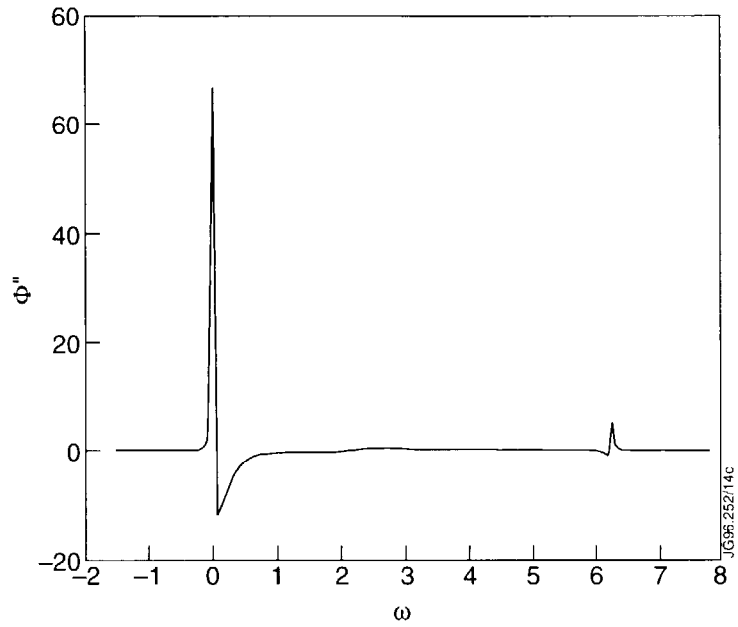

Fig. 13: The second derivative $\frac{\partial^2 \phi}{\partial \omega^2}$ *of the eigenfunction given in fig.12.*

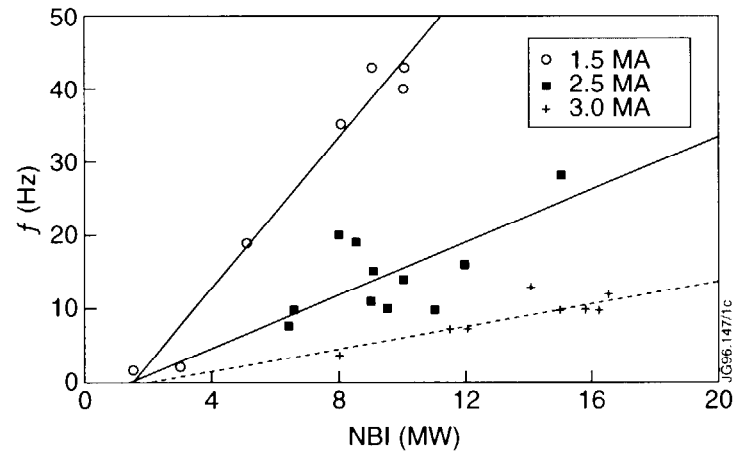

Fig. 14: ELM Frequency plotted as a function of total input power (radiation losses are not taken into account) for a sequence of shots from the 1994-1995 campaign.

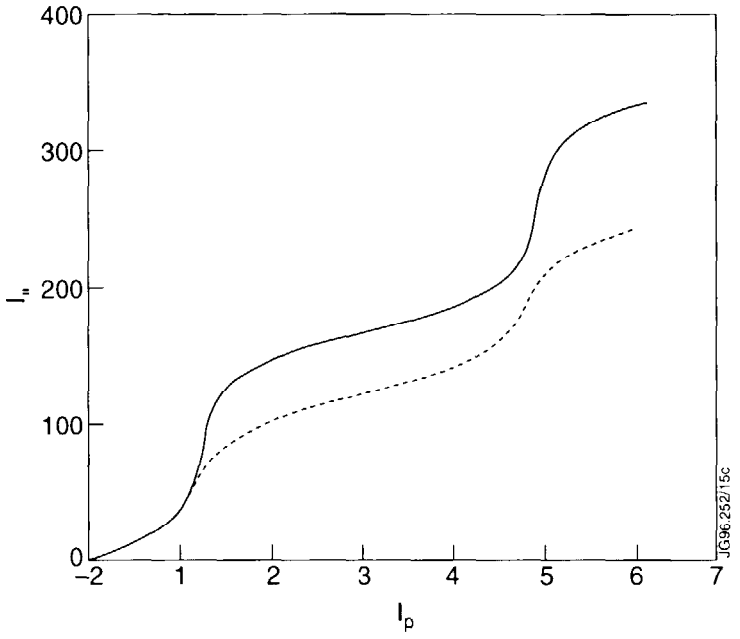

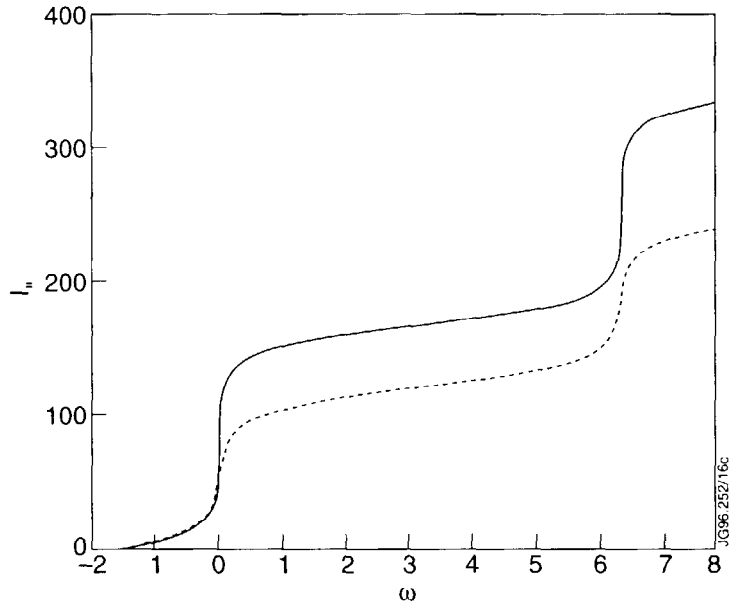

Fig.15a,b: Dependence of the connection length on the poloidal length (top) and on the coordinate ω (bottom), for 2 flux surfaces, viz. ρ = 0.003 (solid curves) and ρ = 0.03 (dashed curves).